Modification of the saddle-point equation for strong-field ionization from atomic *p* orbitals

Xiaodan Mao [1], Kunlong Liu [2,*], Hongcheng Ni [1,3,†] and Jian Wu [1,3,4]

[1] *State Key Laboratory of Precision Spectroscopy, East China Normal University, Shanghai 200241, China*

[2] *School of Physical Sciences, Great Bay University, Dongguan 523000, China*

[3] *Collaborative Innovation Center of Extreme Optics, Shanxi University, Taiyuan, Shanxi 030006, China*

[4] *Chongqing Key Laboratory of Precision Optics, Chongqing Institute of East China Normal University, Chongqing 401121, China*

(Received 14 January 2025; accepted 4 March 2025; published 18 March 2025)

The saddle-point approximation (SPA) within the framework of strong-field approximation is extensively applied in strong-field physics because it offers clear physical insight into intense light-matter interactions. In this study, we introduce an *m*-resolved saddle-point approximation (*m*-SPA), where *m* is the magnetic quantum number, to analyze the ionization dynamics of atoms initially in *p* orbitals subjected to an intense laser field. Our results reveal that *m* influences not only the prefactor of the ionization rate but also the saddle-point equation itself, an effect overlooked in prior studies. The accuracy of the *m*-SPA method is validated through comparisons with the backpropagation method and the strong-field approximation, showing its superiority over the conventional SPA approach. By employing the *m*-SPA approach, we are able to extract more accurate distributions of the initial tunneling exit energy and position, thereby allowing for a more precise determination of the asymptotic photoelectron characteristics. Additionally, we extend the conservation law for angular momentum and energy of photoelectrons from *s* orbitals to *p* orbitals and from circularly polarized to elliptically polarized laser fields, both at the tunnel exit and in the asymptotic region. This work facilitates future research on strong-field ionization from arbitrary atomic orbitals.

DOI: 10.1103/PhysRevA.111.033113

I. INTRODUCTION

Strong-field ionization (SFI) in intense laser fields serves as a fundamental starting point for the in-depth exploration of strong-field physics [1–4]. In the context of SFI for atoms, the initial atomic orbitals play a crucial role [5–11]. For simplicity, however, it has been common practice to assume that photoelectrons ionize from the ground-state *s* orbital in rare gases [12–14]. This simplification overlooks the fact that, with the exception of helium, the outer atomic orbitals of rare gases are actually *p* orbitals, where the bound electrons circulate either clockwise or counterclockwise, depending on their magnetic quantum number *m* [15,16]. When exposed to circularly polarized laser fields, these orbitals exhibit either corotating or counterrotating behavior relative to the laser field. For right circularly polarized laser fields, as used in the present study, p_+ orbitals corotate, while p_- orbitals counterrotate with respect to the laser field. It has been predicted theoretically that the ionization rate for photoelectrons initially counterrotating with respect to the laser field is significantly higher than for the corotating ones [17,18], a finding that was experimentally confirmed by preparing bound electrons in initial *p* orbitals [16,19]. Furthermore, it has been demonstrated that photoelectrons from the $p_\pm$ orbitals exhibit distinct angular distribution offsets, attributable to the deformation of these orbitals under the influence of the laser field [20]. The interaction between diverse initial atomic orbitals and various laser fields, such as intense circularly polarized (CP) fields, elliptically polarized (EP) fields, and two-color fields, has been a focal point of research [15,20,21].

The quantum transition amplitude for the electron from a bound state to a continuum state, under the influence of a strong laser pulse, can be described by the theory of strong-field approximation (SFA) [22–26], which is typically expressed as the time integral of a rapidly oscillating function. With a further saddle-point approximation (SPA) [27–31], this transition can be represented in terms of electron trajectories known as quantum orbits [32], facilitating transparent interpretation of SFI with the language of trajectories. Within the framework of SPA, the transition amplitude is approximated as the product of an exponential integrand evaluated at the saddle-point times and a prefactor. The same approach has been applied to atomic *p* orbitals [9,27,29], where the influence of the magnetic quantum number *m* has been assumed to be encapsulated solely within the prefactor. The exponential integrand and, consequently, the associated saddle-point equation (SPE) are presumed to be independent of *m*.

In this study, we demonstrate that the SPE must be modified to incorporate the magnetic quantum number *m* for *p* orbitals to accurately depict the SFI of these orbitals. We introduce an *m*-resolved saddle-point approximation (*m*-SPA) method to investigate the ionization dynamics of electrons from *p* orbitals in strong CP and EP laser fields. The reliability and accuracy of this method are confirmed through comparisons with results from the backpropagation method [33–36] and the SFA. In the *m*-SPA method, the phase associated with

*Contact author: liukunlong@gbu.edu.cn

†Contact author: hcni@lps.ecnu.edu.cn

the quantum number m in the transition amplitude is incorporated into the phase of the exponential integrand, effectively introducing the influence of m into the SPE. This approach leads to a more nuanced understanding of the dynamics of photoelectrons originating from $p_\pm$ orbitals, both at the tunnel exit and in the asymptotic region. Relative to corotating p_+ photoelectrons, counterrotating p_- photoelectrons are found to be closer to the nucleus at the tunnel exit and have higher tunneling exit energy, which the conventional SPA fails to predict. This allows us to obtain more precise asymptotic dynamics information, including asymptotic momentum and angular momentum. Recently, a subcycle conservation law for angular momentum and energy in SFI was established [37,38], demonstrated through the correlated spectrum of angular momentum and energy (SAME) of photoelectrons at the tunnel exit and in the asymptotic region. With m-SPA, we extend the conservation law to $p_\pm$ orbitals in CP and EP fields, enhancing our understanding of the underlying physical processes in SFI.

This article is organized as follows. In Sec. II, we provide a summary of the theoretical methods utilized in this study, including the backpropagation method, the SFA, the SPA, and the m-SPA. In Sec. III, we perform an in-depth analysis of the SAME and dynamical information of photoelectrons from $p_\pm$ orbitals at the tunnel exit under both CP and EP fields. In Sec. IV, we present the SAME and photoelectron characteristics in the asymptotic region. The conclusion is outlined in Sec. V. Atomic units are used throughout unless stated otherwise.

II. THEORETICAL FRAMEWORK

In this section, we briefly overview the numerical simulation and analytical calculation methods (backpropagation, SFA, SPA, and m-SPA) that are employed to study the ionization dynamics of Ne atoms initially in the $2p$ orbital subjected to intense CP and EP laser fields. In this study, we utilize a laser pulse with the vector potential

$$\boldsymbol{A}(t) = A_0 \cos^4\left(\frac{\omega t}{2N}\right)[\cos(\omega t)\hat{\boldsymbol{e}}_x + \epsilon \sin(\omega t)\hat{\boldsymbol{e}}_y] \quad (1)$$

and the corresponding electric field $\boldsymbol{F}(t) = -\dot{\boldsymbol{A}}(t)$, where A_0 is the amplitude of the vector potential, ω is the central angular frequency, ϵ is the ellipticity, and $N = 10$ is the total number of cycles.

A. The backpropagation method

The backpropagation method [33–36] is a hybrid quantum-classical approach widely applied to retrieve the dynamical characteristics of electrons at the tunnel exit. It involves three steps, including quantum forward propagation using the time-dependent Schrödinger equation (TDSE), transcription of ionized quantum wave packets into classical trajectories, and backpropagation of these classical trajectories along the time axis until a certain stopping criterion is met, which defines the tunnel exit.

We solve the two-dimensional TDSE within the single-active-electron approximation and dipole approximation to analyze the SFI of Ne. The Hamiltonian in the length gauge is given by

$$H = \tfrac{1}{2}p^2 + \boldsymbol{r}\cdot\boldsymbol{F}(t) + V(r), \quad (2)$$

with the Coulomb potential

$$V(r) = -\frac{1 + 9e^{-0.85r^{1.6}}}{\sqrt{r^2 + a_0}}, \quad (3)$$

where the soft-core parameter $a_0 = 3.65$ is tuned to reproduce the ionization potential $I_p = 0.7935$ a.u. for the $2p$ orbital of Ne. The orthogonal normalized eigenfunctions, $\psi_x(\boldsymbol{r})$ and $\psi_y(\boldsymbol{r})$, are obtained using the imaginary-time propagation method, corresponding to the $2p_x$ and $2p_y$ orbitals of Ne, respectively. A linear combination of them yields the initial-state wave function

$$\psi_\pm(\boldsymbol{r}) = \frac{1}{\sqrt{2}}[\psi_x(\boldsymbol{r}) \pm i\psi_y(\boldsymbol{r})], \quad (4)$$

where the subscript $\pm$ denotes the state with the magnetic quantum number $m = \pm 1$.

Employing the split-operator Fourier method, we compute the evolution of the wave function in the laser field. The calculation is performed on a spatial grid comprising 1024 points, with a spatial increment of $\Delta x = \Delta y = 0.2$ a.u. in each of the two dimensions, along with a time step of $\Delta t = 0.02$ a.u. To suppress unphysical reflections of the photoelectron wave packet at the grid boundary, we apply an absorption function near the boundary, $1/[1 + \exp\{(r - r_0)/d\}]$, with the radius parameter $r_0 = 87.4$ a.u. and the width parameter $d = 4$ a.u. As the photoelectron wave packet approaches r_0, we perform absorption on the wave function every 0.2 a.u. in time. The absorbed wave packet is projected onto the Volkov state to obtain the photoelectron momentum distribution.

To convert the ionized quantum wave packet into classical trajectories, we evenly distribute 6000 virtual detectors [39–42] on a spherical shell with a radius of $r_d = 40$ a.u. Following Newton's equation of motion, these classical trajectories are subsequently reversed in time to propagate back until they reach the tunnel exit. Meeting the criterion of zero momentum parallel to the instantaneous electric-field direction during the backward propagation signifies the arrival of the trajectories at the tunnel exit. In our calculations, we have tested that the results converge with respect to the numerical grid parameters.

B. Strong-field approximation

The SFA theory neglects the influence of the laser field on the initial bound state and the effect of the Coulomb interaction on the final continuum state, yielding the transition amplitude in the length gauge [28],

$$\begin{aligned} M_\pm^{\mathrm{SFA}}(\boldsymbol{p}) &= -i\int \langle \boldsymbol{p} + \boldsymbol{A}(t)|\boldsymbol{r}\cdot\boldsymbol{F}(t)|\psi_\pm\rangle e^{iS_0(t)}dt \\ &= -i\int i\frac{\partial}{\partial \boldsymbol{k}}\tilde{\psi}_\pm(\boldsymbol{k})\cdot\boldsymbol{F}(t)e^{iS_0(t)}dt, \end{aligned} \quad (5)$$

where $\boldsymbol{k} = \boldsymbol{p} + \boldsymbol{A}(t)$, the action $S_0(t) = \int^t dt\{[\boldsymbol{p} + \boldsymbol{A}(t)]^2/2 + I_p\}$, and $\tilde{\psi}_\pm(\boldsymbol{k})$ is the Fourier transform of the initial-state wave function, $\tilde{\psi}_\pm(\boldsymbol{k}) = \int d\boldsymbol{r}\exp(i\boldsymbol{k}\cdot\boldsymbol{r})\psi_\pm(\boldsymbol{r})$.

Considering the asymptotic form of the initial wave function in the momentum space [27,43],

$$\tilde{\psi}_{\pm}(\boldsymbol{k}) = \frac{A(-ik)^l}{2^{l+1/2}(2I_p)^{(l-\nu)/2}} \frac{\Gamma(l+\nu+2)}{\Gamma(l+3/2)} \times {}_2F_1\left(\frac{l-\nu}{2}, \frac{l-\nu+1}{2}, l+\frac{3}{2}; -\frac{k^2}{2I_p}\right) \times \frac{Y_{lm}(\hat{\boldsymbol{k}})}{(k^2+2I_p)^{\nu+1}}, \tag{6}$$

where $l = 1$, $m = \pm 1$, $\nu = 1/\sqrt{2I_p}$, $\Gamma(x)$ is the gamma function, Y_{lm} is the spherical harmonics, and ${}_2F_1(a, b, c; z)$ is the Gauss hypergeometric function. For the valence shell of Ne, we have $A = 2.1$ [27]. For computational convenience, the momentum-space wave function [Eq. (6)] of Ne with the $p_{\pm}$ orbitals is approximated as

$$\tilde{\psi}_{\pm}(\boldsymbol{k}) \simeq \frac{k_x + imk_y}{(k^2+2I_p)^{\nu+1}} \quad (m = \pm 1). \tag{7}$$

By substituting this wave function into the transition amplitude [Eq. (5)], we obtain

$$M_{\pm}^{\mathrm{SFA}}(\boldsymbol{p}) = \int f(t) e^{iS_0(t)} dt, \tag{8}$$

where

$$f(t) = \frac{\partial}{\partial \boldsymbol{k}} \left[\frac{k_x + imk_y}{(k^2+2I_p)^{\nu+1}}\right] \cdot \boldsymbol{F}(t). \tag{9}$$

C. Saddle-point approximation

The SPA method effectively transforms the integral in Eq. (8) into a summation over the saddle-point times. Rearranging the prefactor $f(t)$ in the integrand of Eq. (8), we have

$$f(t) = \frac{1}{(k^2+2I_p)^{\nu+2}} f_0(t), \tag{10}$$

with

$$f_0(t) = (F_x + imF_y)(2I_p - \nu k^2) + (-F_x + imF_y)(1+\nu)(k_x + imk_y)^2, \tag{11}$$

and the transition amplitude [Eq. (8)] can then be written as

$$M_{\pm}^{\mathrm{SPA}}(\boldsymbol{p}) \approx \sum_{t_s} f_0(t_s) |\ddot{S}_0(t_s)|^{-(\nu+3)/2} e^{iS_0(t_s)}, \tag{12}$$

where we have used [27,29,43]

$$\int_C \frac{e^{iS_0(z)}}{[\dot{S}_0(z)]^{\nu}} dz \approx i^{\nu} \frac{\Gamma(\nu/2)}{2\Gamma(\nu)} \sum_j \sqrt{2\pi i} (-2i)^{\nu/2} \times |\ddot{S}_0(z_j)|^{-(\nu+1)/2} e^{iS_0(z_j)}. \tag{13}$$

Here, the action

$$S_0(t_s) = -\int_{t_s}^{t_r} dt \left\{\frac{1}{2}[\boldsymbol{p} + \boldsymbol{A}(t)]^2 + I_p\right\}, \tag{14}$$

and complex saddle-point time $t_s = t_r + it_i$ is obtained by solving the SPE,

$$-\dot{S}_0 = \tfrac{1}{2}[\boldsymbol{p} + \boldsymbol{A}(t_s)]^2 + I_p = 0, \tag{15}$$

where t_r represents the ionization time and t_i is related to the tunneling ionization rate.

We reorganize the SPE [Eq. (15)] to isolate its imaginary part

$$i[\boldsymbol{p}_{\perp} + \mathrm{Re}\boldsymbol{A}(t_s)] \cdot \mathrm{Im}\boldsymbol{A}(t_s) = 0, \tag{16}$$

where $\boldsymbol{p}_{\perp} = (p_x, p_y)$ is the component of $\boldsymbol{p}$ in the laser polarization plane. From this expression, it is clear that $\boldsymbol{p}_{\perp} + \mathrm{Re}\boldsymbol{A}(t_s)$ is perpendicular to $\mathrm{Im}\boldsymbol{A}(t_s) = (\mathrm{Im}A_x(t_s), \mathrm{Im}A_y(t_s))$. Therefore, $\boldsymbol{p}_{\perp} + \mathrm{Re}\boldsymbol{A}(t_s)$ has a direction along the unit vector

$$\hat{\boldsymbol{k}}_{\perp} = \frac{-\mathrm{Im}A_y(t_s)\hat{\boldsymbol{e}}_x + \mathrm{Im}A_x(t_s)\hat{\boldsymbol{e}}_y}{\sqrt{[\mathrm{Im}A_x(t_s)]^2 + [\mathrm{Im}A_y(t_s)]^2}}. \tag{17}$$

Hence, with the introduction of an auxiliary momentum as

$$k_{\perp} = [\boldsymbol{p}_{\perp} + \mathrm{Re}\boldsymbol{A}(t_s)] \cdot \frac{-\mathrm{Im}A_y(t_s)\hat{\boldsymbol{e}}_x + \mathrm{Im}A_x(t_s)\hat{\boldsymbol{e}}_y}{\sqrt{[\mathrm{Im}A_x(t_s)]^2 + [\mathrm{Im}A_y(t_s)]^2}}, \tag{18}$$

Eq. (16) is then fulfilled automatically. This procedure significantly reduces the search range for the saddle-point times from the entire complex plane to just one axis, thus greatly diminishing the computational complexity [44–47]. Furthermore, as the calculation is performed in the $(t_r, k_{\perp})$ coordinate system, the Jacobian factor must be included when calculating the ionization rate:

$$W_{\pm}^{\mathrm{SPA}}(t_r, k_{\perp}) = \left|\det \frac{\partial(p_x, p_y)}{\partial(t_r, k_{\perp})}\right| |M_{\pm}^{\mathrm{SPA}}(\boldsymbol{p})|^2. \tag{19}$$

D. *m*-resolved saddle-point approximation

The SPA approach traditionally considers only the effect of the magnetic quantum number m on the prefactor $f_0(t_s)$ of the transition amplitude. However, as we will demonstrate later, this approach leads to inaccuracies in both the tunneling exit characteristics and the asymptotic behavior of the photoelectrons. To fully incorporate the effect of m on the SPE, we introduce the m-SPA method. We begin by processing the field-related integrand in Eq. (10):

$$F_x(t) + imF_y(t) = -imF(t)e^{im\phi_F} \quad (m = \pm 1), \tag{20}$$

$$-F_x(t) + imF_y(t) = -imF(t)e^{-im\phi_F} \quad (m = \pm 1), \tag{21}$$

where $F(t) = \sqrt{F_x^2(t) + F_y^2(t)}$ is the magnitude of the electric field and

$$\phi_F = \arctan\left(\frac{F_x(t)}{-F_y(t)}\right). \tag{22}$$

Thus, Eq. (10) can be rewritten as

$$f(t) = f_m(t)e^{im\phi_F}, \tag{23}$$

where

$$f_m(t) = \frac{-imF}{(k^2+2I_p)^{\nu+2}} [2I_p - \nu k^2 + (1+\nu)(k_x + imk_y)^2 e^{-2im\phi_F}]. \tag{24}$$

In Eq. (8), the two exponential terms can then be combined into one, yielding

$$e^{im\phi_F} e^{iS_0(t)} = e^{iS_m(t)}, \tag{25}$$

where $S_m(t) = S_0(t) + m\phi_F$. Since the term $f_m(t)$ remains slowly varying relative to the action term $S_m(t)$ at the saddle point, we can use the SPA [27,43]

$$\int_C e^{iS(z)}dz \approx \sum_j \sqrt{2\pi i}|\ddot{S}|^{-1/2}e^{iS(z_j)} \tag{26}$$

to calculate Eq. (8), leading to

$$M_{\pm}^{m\text{-SPA}}(\boldsymbol{p}) \approx \sum_{t_s} f_m(t_s)|\ddot{S}_m(t_s)|^{-1/2}e^{iS_m(t_s)}, \tag{27}$$

where the saddle-point time t_s is determined by solving the m-resolved saddle-point equation (m-SPE),

$$-\dot{S}_m = \tfrac{1}{2}[\boldsymbol{p} + \boldsymbol{A}(t_s)]^2 + I_p + m\dot{\phi}_F = 0, \tag{28}$$

where, for long pulses,

$$\dot{\phi}_F = \frac{\epsilon\omega}{\epsilon^2\cos^2(\omega t) + \sin^2(\omega t)}. \tag{29}$$

In CP fields, $\dot{\phi}_F = \epsilon\omega$, with $\epsilon = \pm 1$, whereas in EP fields, the ionization rate peaks at the maxima of the laser electric field $t = t_0 = \pi/(2\omega)$, leading to $\dot{\phi}_F \approx \epsilon\omega$. The m-SPE [Eq. (28)] is then approximated as

$$-\dot{S}_m = \tfrac{1}{2}[\boldsymbol{p} + \boldsymbol{A}(t_s)]^2 + I_p + m\epsilon\omega = 0. \tag{30}$$

The subsequent procedure follows the same steps as in the SPA method. In addition, the present scheme is readily extensible to higher values of $|m|$. For the SFI of electrons from orbitals where the magnetic quantum number $|m| > 1$, we can follow the same procedure by incorporating m into the phase $S_0(t)$, leading to the same m-SPE [Eq. (30)].

III. THE TUNNELING REGION

In this section, we delve into the tunneling dynamics of Ne $p_{\pm}$ orbitals under the influence of intense CP and EP laser fields, focusing on the characteristics at the tunnel exit. To validate our proposed m-SPA method and compare it with the traditional SPA approach, we use the tunneling characteristics extracted with the backpropagation method [33–36] as our reference standard. The backpropagation method treats the tunneling dynamics fully quantum mechanically and retrieves the tunneling exit characteristics from the portion of the wave function that eventually ionizes. It does so by backpropagating along the time axis using classical electron trajectories, a method proven to be reliable for obtaining highly differential information about the tunnel exit. This method has been widely utilized in various studies, such as identifying the origin of tunneling time delays [34,48], extracting the tunneling [49,50] and deformation [20] dynamics of atomic p orbitals, probing backward rescattering times [51], discovering new conservation laws [37,38], and investigating the subcycle transfer of linear momentum [52] due to nondipole effects [53–55].

To benchmark the m-SPA method, we find it advantageous to utilize the subcycle conservation law that relates angular momentum and energy, as reflected in the SAME, in intense CP fields [37,38]:

$$E_0 = \epsilon\omega(L_{z0} - m) - I_p \quad (\epsilon = \pm 1), \tag{31}$$

where E_0 represents the total energy of the electron at the tunnel exit, L_{z0} denotes its angular momentum, and $\epsilon = +1$ stands for the right-circularly polarized (RCP) pulse, while $\epsilon = -1$ denotes the left-circularly polarized pulse. This conservation law holds at any moment within the laser pulse, which stems from the infinite-order continuous dynamical rotational symmetry present in CP fields [37], or can alternatively be understood within the rotating frame [38]. Based on this conservation law, one can deduce that for the subset of electrons that tunnel adiabatically with $E_0 = -I_p$, their initial magnetic quantum number is mirrored in the initial angular momentum at the tunnel exit, that is, $L_{z0} = m$. A detailed derivation of the conservation law [Eq. (31)] can be found in Appendix A.

We present in Fig. 1 a comparative analysis of the tunneling exit characteristics derived from the backpropagation method [Figs. 1(a1)–1(a5)], the m-SPA method [Figs. 1(b1)–1(b5)], and the conventional SPA approach [Figs. 1(c1)–1(c5)], encompassing various aspects at the tunnel exit subjected to a RCP laser field. Specifically, the comparison covers the conservation law between angular momentum and energy, as reflected in the SAME, for the p_+ orbital (first column) and the p_- orbital (second column), the distribution of the initial angular momentum (third column), tunneling exit energy (fourth column), and tunneling exit position (fifth column).

In the first and second columns in Fig. 1, the three black dotted lines represent the conservation law as presented in Eq. (31), corresponding to $m = -1$, $m = 0$, and $m = +1$ from top to bottom in each panel. Upon comparing Figs. 1(a1) and 1(a2), it is evident that the conservation law [Eq. (31)] is satisfied. The slight curvature and downward shift observed are attributed to the influence of the Coulomb potential in the final state [37]. Clearly, as depicted in Figs. 1(b1) and 1(b2), the m-SPA method accurately reproduces the conservation law. In contrast, as demonstrated in Figs. 1(c1) and 1(c2), the conventional SPA approach fails to reproduce the m-dependent conservation law.

We now examine additional tunneling exit characteristics. As observed in Fig. 1(a3), the average initial angular momentum for the p_+ orbital $\langle L_{z0}\rangle_+$ is approximately 3.6. Compared to adiabatic tunneling for the p_+ orbital, $L_{z0} = 1$, this value suggests that on average, 2.6 photons are absorbed during the under-barrier tunneling process. In contrast, for the p_- orbital, $\langle L_{z0}\rangle_-$ is approximately 2.2. Compared to its adiabatic tunneling, $L_{z0} = -1$, this value indicates that on average, 3.2 photons are absorbed during tunneling. Consequently, the p_- orbital exhibits a higher tunneling exit energy than the p_+ orbital, as clearly depicted in Fig. 1(a4). The higher tunneling exit energy and greater number of photons absorbed by the p_- orbital also lead to a closer tunneling exit position for the p_- orbital compared to the p_+ orbital. It is important to note that, under the RCP pulse used in this context, the p_+ orbital corotates with the RCP pulse, while the p_- orbital counterrotates. Therefore, these observations align with the established understanding that counterrotating orbitals are more susceptible to ionization and thus have a higher ionization probability. Obviously, all these characteristics are accurately captured by the m-SPA method. The minor discrepancies in the tunneling exit energy and position can be attributed to the Coulomb interaction, which is included in the full backpropagation

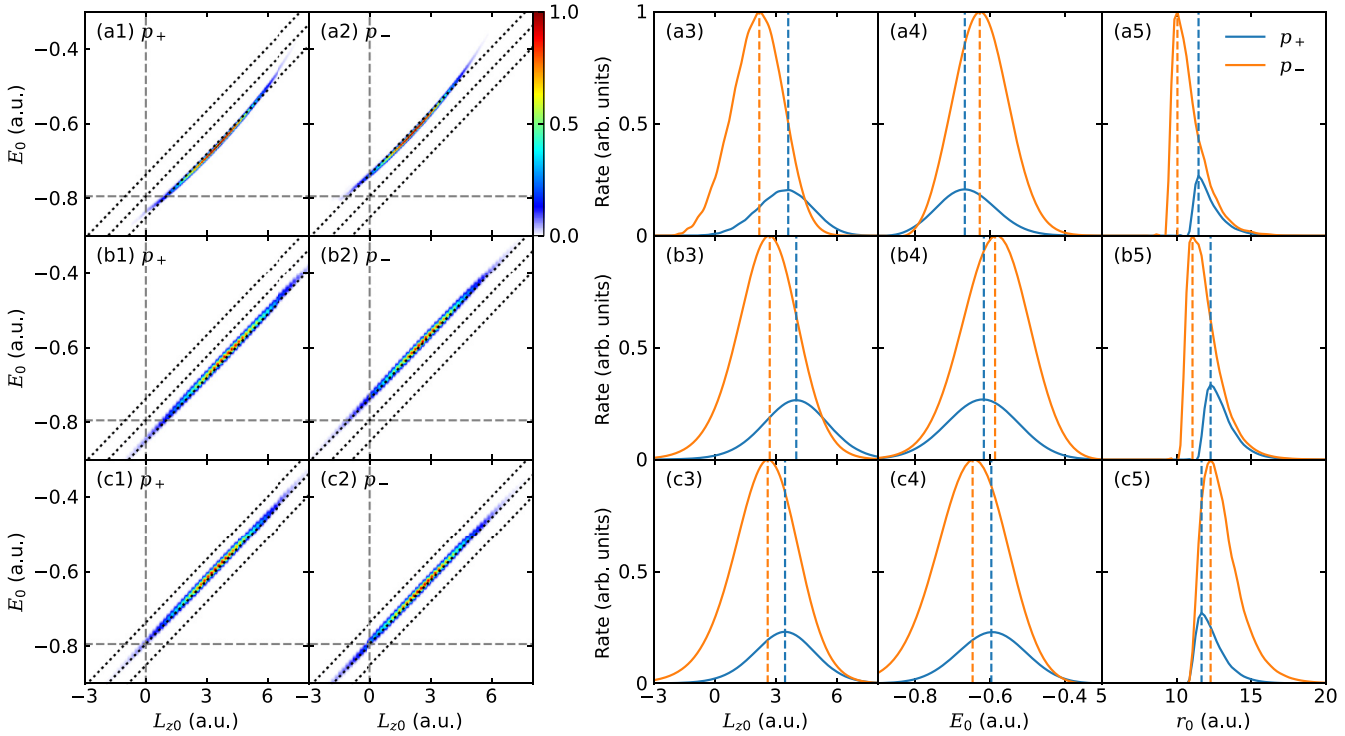

FIG. 1. Correlated spectrum of angular momentum and energy (SAME; first column for p_+ and second column for p_-), angular momentum distribution (third column), energy distribution (fourth column), and initial position distribution (fifth column) at the tunnel exit for photoelectrons ionized from $p_\pm$ orbitals of Ne in the RCP field, calculated by (a1)–(a5) backpropagation, (b1)–(b5) m-SPA, and (c1)–(c5) SPA. Solid blue lines correspond to the p_+ orbital, and solid orange lines represent the p_- orbital in the last three columns. The gray dashed lines mark the position of $L_{z0} = 0$ and $E_0 = -I_p$, the colored vertical dashed lines represent the peak position of the respective distribution, and the black dotted lines denote Eq. (31) with $m = -1, 0, 1$ from top to bottom in each panel. In the simulation, the peak laser intensity $I_0 = 2 \times 10^{14}$ W/cm^2, the wavelength $\lambda = 800$ nm, and the ellipticity $\epsilon = 1$.

method but not in SFA-derived methods. We note that the m-SPA approach provides the correct initial tunneling conditions, which is beneficial for classical trajectory simulations. In contrast, the conventional SPA fails to reproduce the correct orders of the peaks in the tunneling exit energy and position for the p_+ and p_- orbitals.

We now turn our attention to the tunneling exit characteristics in a right-elliptically polarized (REP) laser field. A comparative analysis using the backpropagation method, m-SPA, and SPA is presented in Fig. 2. It is evident that the same conclusions drawn from the RCP field case apply here: Counterrotating orbitals are more readily ionized, resulting in a greater number of absorbed photons, higher tunneling exit energy, and a closer tunneling exit position compared to those of corotating orbitals. Consistently, the m-SPA method accurately reproduces the backpropagation results, while the conventional SPA method does not. A distinct difference between EP and CP pulses is that the conservation law relating angular momentum and energy is no longer linear for EP pulses. As previously indicated [36], the instantaneous effective angular frequency for the EP pulse varies with time, leading to a changing slope of the SAME at different moments within the laser pulse. This results in a curved relationship between angular momentum and energy, which lacks a simple closed-form analytical expression. Specifically, the angular momentum and energy are interconnected through their parametric dependence on the auxiliary momentum k [Eq. (18)]. The detailed conservation law at the tunnel exit for EP pulses is elaborated in Appendix A.

IV. THE ASYMPTOTIC REGION

In this section, we delve into the ionization of Ne $p_\pm$ orbitals under CP and EP fields, with a particular focus on the photoelectron characteristics in the asymptotic region. We employ the SFA in its direct integral form as our benchmark. Since the m-SPA and SPA are approximations that build upon the SFA, comparing their results to those of the SFA provides insights into how the saddle-point approximation should be applied to the SFA and how the corresponding SPE should be formulated.

In the asymptotic region, a similar conservation law can be identified for CP pulses [37,38]:

$$E = \epsilon\omega(L_z - m) - I_p - U_p \quad (\epsilon = \pm 1). \tag{32}$$

Compared to the conservation law at the tunnel exit [Eq. (31)], an additional term, $-U_p$, is present. This term has been demonstrated to arise from the exchange of photons of the ionized electron with the laser field after tunneling until it reaches the detector in the asymptotic region [37]. The derivation of the conservation law is outlined in Appendix B. This conservation law also aligns well with the energy expression for above-threshold ionization (ATI). By substituting $\epsilon(L_z - m)$ with the number of photons absorbed n, the

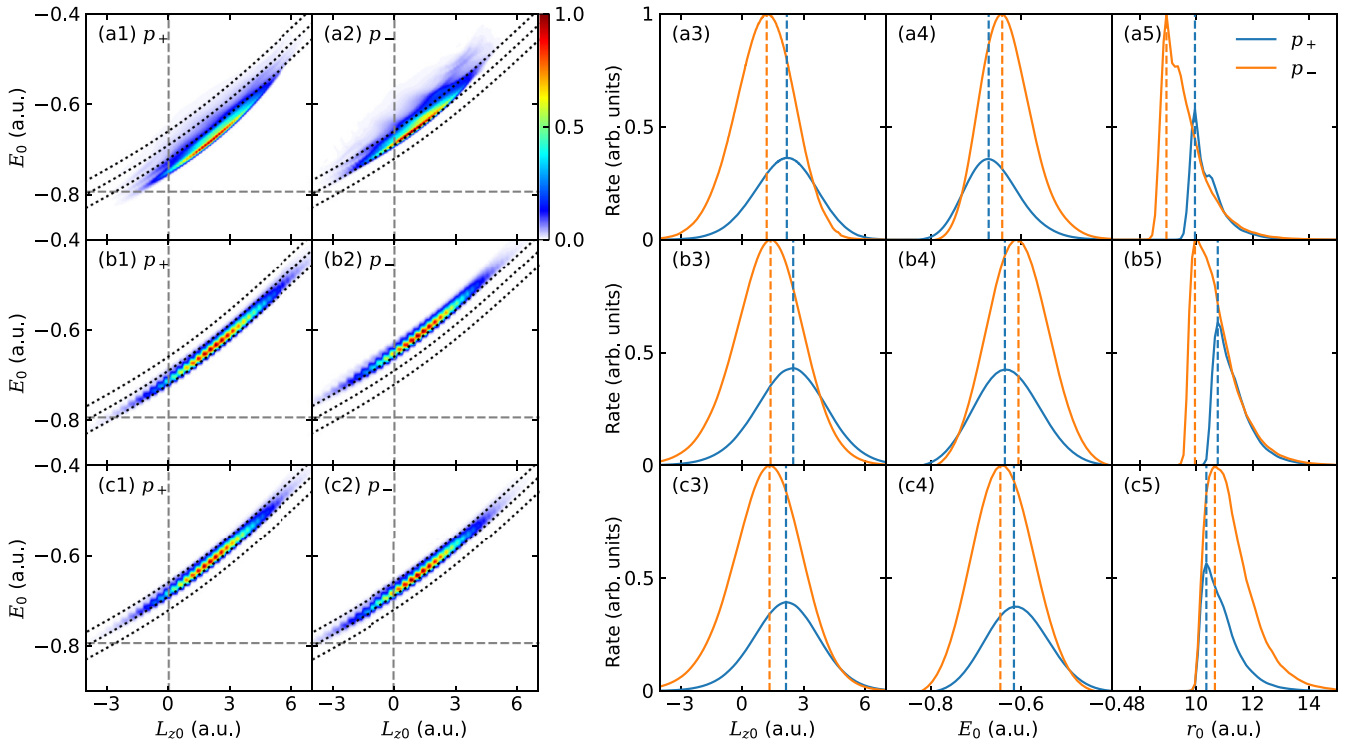

FIG. 2. The same as Fig. 1, but for the REP field with an ellipticity $\epsilon = 0.7$. The black dotted lines denote the conservation law for the angular momentum and energy given by their parametric dependence on k in Eqs. (A11) and (A12) with $m = -1, 0, 1$ from top to bottom in each panel.

expression reduces to the familiar expression for the energy of ATI:

$$E = n\omega - I_p - U_p. \tag{33}$$

In Fig. 3, we present a comparative analysis of the asymptotic photoelectron characteristics obtained from three different methods when the atom is subjected to a RCP laser field: the SFA method [Figs. 3(a1)–3(a5)], the m-SPA method [Figs. 3(b1)–3(b5)], and the conventional SPA approach [Figs. 3(c1)–3(c5)]. The comparison encompasses the conservation law between asymptotic angular momentum and energy, as reflected in the SAME, for the p_+ orbital (first column) and the p_- orbital (second column), the distribution of the final angular momentum (third column), energy (fourth column), and radial momentum (fifth column). This comparison allows for a detailed evaluation of how each method performs in capturing the essential dynamics of photoelectrons in the asymptotic region, providing insights into their relative accuracy and reliability.

In the first and second columns of Fig. 3, the three black dotted lines represent the conservation law as given by Eq. (32), corresponding to $m = -1$, $m = 0$, and $m = +1$ from top to bottom in each panel. By examining Figs. 3(a1) and 3(a2), it is clear that the conservation law [Eq. (32)] for the asymptotic region holds true. The discontinuous distribution observed in these plots is due to the different orders of ATI rings, which result from intercycle interferences. Evidently, as shown in Figs. 3(b1) and 3(b2), the m-SPA method faithfully reproduces the conservation law. In contrast, as illustrated in Figs. 3(c1) and 3(c2), the conventional SPA approach fails to capture the conservation law.

Regarding the final energy and radial momentum distribution, as depicted in the fourth and fifth columns of Fig. 3, there are no significant differences observed across the methods presented in Figs. 3(a) to 3(c). This is because the final momentum $\boldsymbol{p}$ is approximately given by

$$\boldsymbol{p} = \boldsymbol{k} - \boldsymbol{A}(t), \tag{34}$$

which is predominantly determined by the vector potential, which is relatively large compared to the initial momentum $\boldsymbol{k}$ at the tunnel exit. However, the final angular momentum distribution shows considerable variation. By comparing Figs. 3(a3), 3(b3), and 3(c3), it can be concluded that the m-SPA method accurately reproduces the results of the SFA, while the conventional SPA fails to yield the correct outcome. It is important to note that angular momentum is related to the phase gradient in the angular direction, given that the angular momentum operator is $\hat{L}_z = -i\frac{\partial}{\partial\phi}$. The inability of the SPA to reproduce the angular momentum distribution suggests that the phase of the photoelectron momentum distribution obtained by SPA is incorrect, even though the amplitude is reasonably accurate. Consequently, SPA would be ineffective in scenarios where quantum interference is particularly prominent.

By comparing Fig. 3 to Fig. 1, we gain insights into the continuum motion following electron tunneling. As shown in Fig. 1(a3), the p_+ electron absorbs approximately 2.6 photons during tunneling, reaching $\langle L_{z0}\rangle_+ \approx 3.6$. After

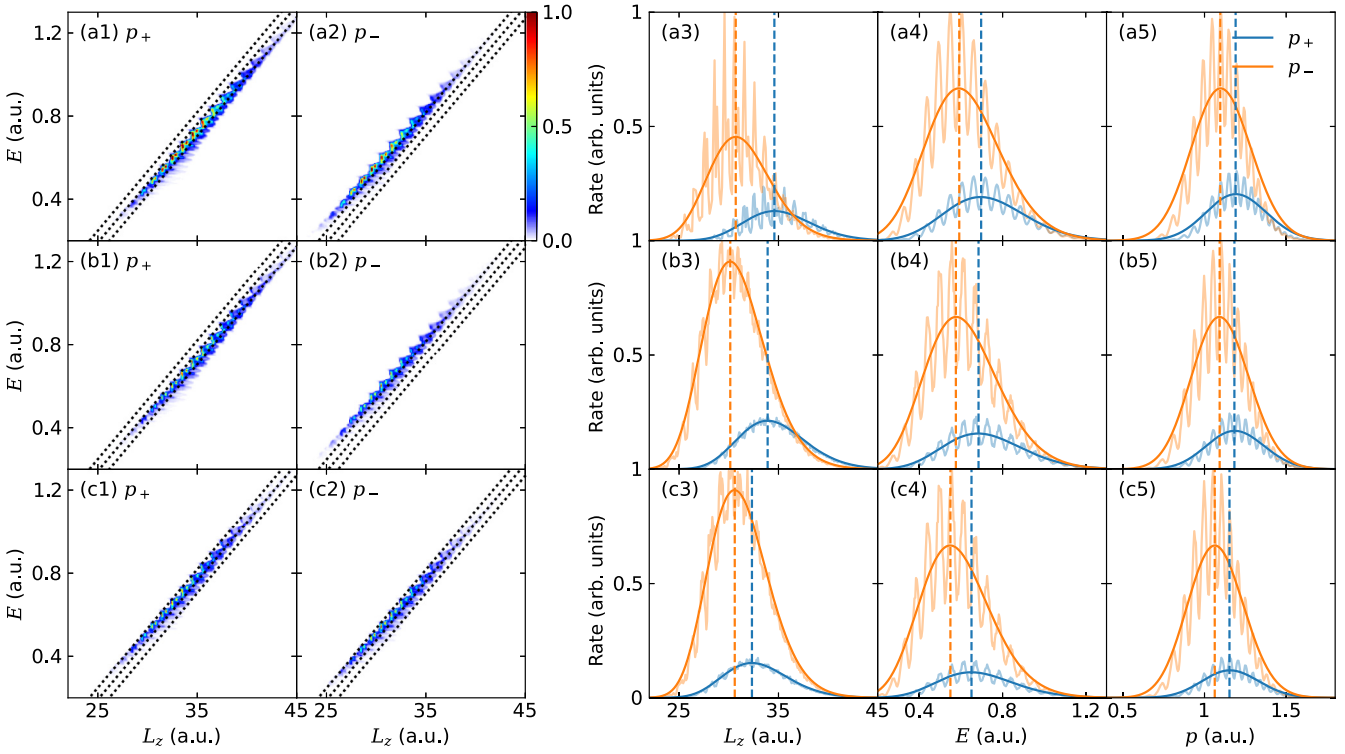

FIG. 3. Correlated SAME (first column for p_+ and second column for p_-), angular momentum distribution (third column), energy distribution fourth column)), and radial momentum distribution (fifth column) in the asymptotic region for photoelectrons ionized from $p_\pm$ orbitals of Ne in the RCP field, calculated by (a1)–(a5) SFA, (b1)–(b5) m-SPA, and (c1)–(c5) SPA. In the last three columns, the blue lines correspond to the p_+ orbital, and the orange lines represent the p_- orbital, with light-colored lines showing calculation results from various methods and dark-colored lines indicating the fits to the light-colored lines. The vertical dashed lines represent the peak position of the respective distribution, and the black dotted lines denote Eq. (32) with $m = -1, 0, 1$ from top to bottom in each panel. In the simulation, the peak laser intensity $I_0 = 2 \times 10^{14}$ W/cm^2, the wavelength $\lambda = 800$ nm, and the ellipticity $\epsilon = 1$.

tunneling, it absorbs, on average, an additional 31 photons, reaching $\langle L_z\rangle_+ \approx 34.6$ asymptotically, which is evident from Fig. 3(a3). In contrast, the p_- electron absorbs about 3.2 photons during tunneling, reaching $\langle L_{z0}\rangle_- \approx 2.2$. After tunneling, it absorbs, on average, another 29.5 photons, resulting in $\langle L_z\rangle_- \approx 31.7$ asymptotically. Notably, while the counterrotating p_- orbital absorbs more photons or energy during tunneling, it absorbs fewer photons or energy after tunneling in the continuum motion. This can be understood within the simple physical picture according to Eq. (34). Although the p_- electron absorbs, on average, 0.6 photon more from the field than the p_+ electron, it still has a smaller average initial transverse momentum than the p_+ electron since its $\langle L_{z0}\rangle$ is less, which implies $\langle k_+\rangle > \langle k_-\rangle$. According to Eq. (34), the average energy absorbed during the continuum motion ΔE can be expressed as

$$\begin{aligned}\langle \Delta E\rangle &= \tfrac{1}{2}\langle p^2 - k^2\rangle = \tfrac{1}{2}\langle (\boldsymbol{k}-\boldsymbol{A})^2 - k^2\rangle = -\langle \boldsymbol{k}\rangle\cdot\boldsymbol{A} + \tfrac{1}{2}A_0^2 \\ &= \langle k\rangle A_0 + \tfrac{1}{2}A_0^2, \end{aligned} \tag{35}$$

where the last equation uses the fact that the average initial momentum at the tunnel exit is antiparallel to the instantaneous vector potential. Since $\langle k_+\rangle > \langle k_-\rangle$, it follows that $\langle \Delta E_+\rangle > \langle \Delta E_-\rangle$.

In addition, we can analyze the asymptotic characteristics of electrons from the $p_\pm$ orbitals in the REP field, as shown in Fig. 4. It is evident that our m-SPA method is also applicable to EP pulses. Furthermore, the conservation law for the EP pulse exhibits a curved pattern in the asymptotic region. Once again, the angular momentum and energy are linked to each other through their parametric dependence on the auxiliary momentum k [Eq. (18)], with the detailed relationship provided in Appendix B. The black dotted lines in Figs. 4(a) and 4(b) represent the conservation law corresponding to $m = -1$ and $m = +1$ from top to bottom in each panel, while those in Fig. 4(c) correspond to $m = 0$. The broadening of the SAME distribution is due to the varying laser amplitude at different time instances. As demonstrated in the insets of Figs. 4(a1) and 4(a2), the SAME at the pulse peak ($t = t_0$) coincides precisely with the black dotted lines. The same conclusion can be reached using the m-SPA method, whereas the conventional SPA fails to replicate the correct outcome.

V. CONCLUSIONS

In conclusion, we developed and validated an m-resolved saddle-point approximation method that accounts for the magnetic quantum number m in the saddle-point equation for strong-field ionization of atoms initially in p orbitals. The m-SPA method provides a more accurate representation of the ionization dynamics by correctly incorporating the influence of m on the SPE, leading to improved predictions of the initial tunneling position, angular momentum, and energy distribution of the photoelectron. Our findings reveal that

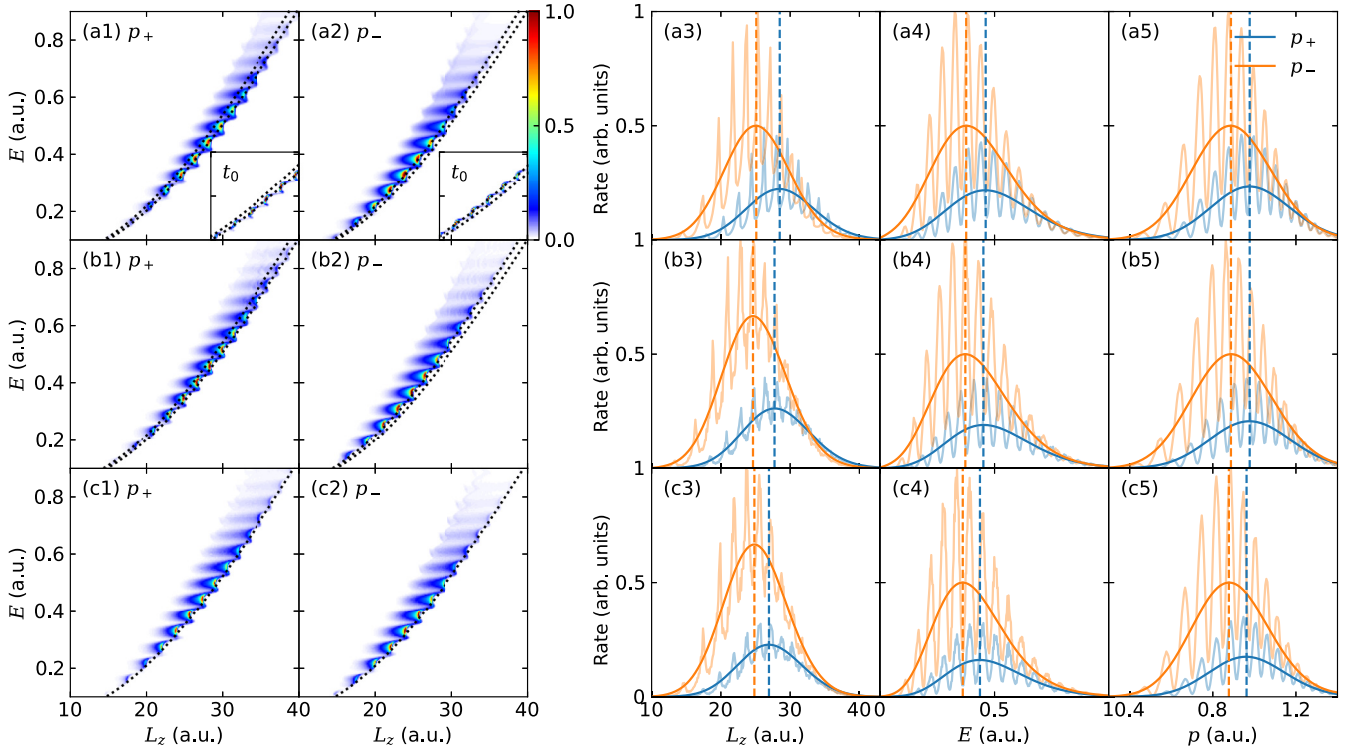

FIG. 4. The same as Fig. 3, but for the REP field with an ellipticity $\epsilon = 0.7$. The black dotted lines denote the conservation law for the angular momentum and energy given by their parametric dependence on k in Eqs. (B7) and (B8) with $m = -1, 1$ from top to bottom in (a) and (b) and $m = 0$ in (c). The insets illustrate the SAME at the pulse center ($t = t_0$).

photoelectrons from the counterrotating p_- orbital ionize at higher rates and from positions closer to the nucleus and absorb more photons during under-barrier tunneling, compared to those from the corotating p_+ orbital, resulting in distinct angular momentum and energy distributions at the tunnel exit. The m-SPA method allows for a more precise calculation of the asymptotic photoelectron characteristics as well and also enables the generalization of angular momentum and energy conservation laws to p orbitals in both circularly and elliptically polarized fields, both at the tunnel exit and in the asymptotic region. The m-SPA is readily extensible to even higher m quantum numbers, such as $d_{\pm 2}$ orbitals. This study broadens our perspective on the dynamic characteristics of photoelectrons from various orbitals and enhances the accuracy and reliability of theoretical predictions for strong-field physics, paving the way for future research starting from arbitrary atomic orbitals.

ACKNOWLEDGMENTS

We would like to thank S. Eckart for helpful discussions. This work was supported by the National Natural Science Foundation of China (Grants No. 92150105, No. 12474341, No. 12174133, No. 12227807, and No. 12241407), the Science and Technology Commission of Shanghai Municipality (Grant No. 23JC1402000), and the Shanghai Pilot Program for Basic Research (Grant No. TQ20240204). Numerical computations were in part performed on the ECNU Multi-functional Platform for Innovation (001).

DATA AVAILABILITY

The data that support the findings of this article are openly available [56].

APPENDIX A: CONSERVATION LAW AT THE TUNNEL EXIT

In this Appendix, we provide a derivation of the analytical expression of the conservation law for angular momentum and energy at the tunnel exit. For simplicity, we consider the scenario in which long pulses are used, thus neglecting the temporal envelope effect in our calculations. By substituting the vector potential from Eq. (1) into the m-SPE given by Eq. (30), we can obtain its imaginary part

$$A_0^2 \cos(\omega t_r)\sin(\omega t_r)\cosh(\omega t_i)\sinh(\omega t_i)(\epsilon^2 - 1) + A_0 \sinh(\omega t_i)[-p_x \sin(\omega t_r) + \epsilon p_y \cos(\omega t_r)] = 0 \quad \text{(A1)}$$

and real part

$$A_0^2 \cosh^2(\omega t_i)[\cos^2(\omega t_r) + \epsilon^2 \sin^2(\omega t_r)] - A_0^2 \sinh^2(\omega t_i)[\sin^2(\omega t_r) + \epsilon^2 \cos^2(\omega t_r)] + 2A_0 \cosh(\omega t_i)[p_x \cos(\omega t_r) + \epsilon p_y \sin(\omega t_r)] + p^2 + 2I_p' = 0, \quad \text{(A2)}$$

where the effective ionization potential $I_p' = I_p + m\epsilon\omega$.

For CP fields ($\epsilon = \pm 1$), Eqs. (A1) and (A2) reduce to

$$t_r = \frac{1}{\epsilon\omega}\left[\arctan\left(\frac{p_y}{p_x}\right) + \pi\right], \tag{A3}$$

$$t_i = \frac{1}{\omega}\text{arccosh}\left(\frac{E + I_p' + U_p}{A_0 p}\right), \tag{A4}$$

where $E = p^2/2$ is the energy, $p = \sqrt{p_x^2 + p_y^2}$ is the asymptotic momentum, and $U_p = A_0^2/2$ is the ponderomotive energy. The tunneling exit position is given by

$$\begin{aligned}\boldsymbol{r}_0 &= \text{Re}\int_{t_s}^{t_r} dt[\boldsymbol{p} + \boldsymbol{A}(t)] = \text{Im}\int_0^{t_i} dt\boldsymbol{A}(t_r + it) \\ &= \frac{E + I_p' + U_p - A_0 p}{\epsilon\omega p^2}(p_y\hat{\boldsymbol{e}}_x - p_x\hat{\boldsymbol{e}}_y),\end{aligned} \tag{A5}$$

and the initial momentum is

$$\boldsymbol{k} = \boldsymbol{p} + \boldsymbol{A}(t_r) = \left(1 - \frac{A_0}{p}\right)\boldsymbol{p}. \tag{A6}$$

Thus, we can obtain the initial angular momentum

$$\boldsymbol{L}_0 = \boldsymbol{r}_0 \times \boldsymbol{k} = \left(1 - \frac{A_0}{p}\right)\frac{E + I_p' + U_p - A_0 p}{\epsilon\omega}\hat{\boldsymbol{e}}_z \tag{A7}$$

and the tunneling exit energy

$$\begin{aligned}E_0 &= \frac{1}{2}k^2 + \boldsymbol{r}_0 \cdot \boldsymbol{F}(t_r) \\ &= \left(1 - \frac{A_0}{p}\right)(E + I_p' + U_p - A_0 p) - I_p' \\ &= \epsilon\omega L_{z0} - I_p' \\ &= \epsilon\omega(L_{z0} - m) - I_p.\end{aligned} \tag{A8}$$

Clearly, the conservation law for angular momentum and energy associated with the magnetic quantum number m at the tunnel exit in CP fields is given by

$$E_0 = \epsilon\omega(L_{z0} - m) - I_p. \tag{A9}$$

For EP fields, we focus only on ionization that occurs at the peak of the electric field of the laser. It is not difficult to obtain the expression for the tunneling exit position,

$$x_0 = \frac{\epsilon k - A_0 + \sqrt{k^2 - 2kA_0\epsilon + 2I_p'(1 - \epsilon^2) + A_0^2}}{\omega(\epsilon^2 - 1)}, \tag{A10}$$

the initial angular momentum

$$L_{z0} = x_0 k, \tag{A11}$$

and the tunneling exit energy

$$E_0 = \tfrac{1}{2}k^2 + x_0 A_0\omega. \tag{A12}$$

In EP fields, the conservation law for angular momentum and energy associated with the magnetic quantum number m at the tunnel exit is thus established through the dependence of the angular momentum and energy on the auxiliary momentum k, given by Eqs. (A11) and (A12).

APPENDIX B: CONSERVATION LAW IN THE ASYMPTOTIC REGION

In this Appendix, we derive the analytical expression for the conservation law for angular momentum and energy in the asymptotic region, where long-pulse approximation is used. At the end of the laser field, the final position is given by

$$\begin{aligned}\boldsymbol{r}_f &= \boldsymbol{r}_0 + \int_{t_r}^{t_f} dt[\boldsymbol{p} + \boldsymbol{A}(t)] \\ &= \boldsymbol{r}_0 + [\boldsymbol{k} - \boldsymbol{A}(t_r)](t_f - t_r) + \int_{t_r}^{t_f} \boldsymbol{A}(t)dt,\end{aligned} \tag{B1}$$

and the final momentum is

$$\boldsymbol{p} = \boldsymbol{k} - \boldsymbol{A}(t_r), \tag{B2}$$

resulting in the final angular momentum

$$\boldsymbol{L} = \boldsymbol{r}_f \times \boldsymbol{p} = \left[\boldsymbol{r}_0 + \int_{t_r}^{t_f} \boldsymbol{A}(t)dt\right] \times [\boldsymbol{k} - \boldsymbol{A}(t_r)] \tag{B3}$$

and the final energy

$$E = \tfrac{1}{2}p^2 = \tfrac{1}{2}[\boldsymbol{k} - \boldsymbol{A}(t_r)]^2. \tag{B4}$$

For CP fields ($\epsilon = \pm 1$), the final angular momentum becomes

$$\begin{aligned}\boldsymbol{L} &= \left(\boldsymbol{r}_0 - \frac{\boldsymbol{F}}{\omega^2}\right) \times [\boldsymbol{k} - \boldsymbol{A}(t_r)] \\ &= \left(\frac{E + I_p' + U_p - A_0 p}{\epsilon\omega} + \frac{A_0 p}{\epsilon\omega}\right)\hat{\boldsymbol{e}}_z \\ &= \frac{E + I_p' + U_p}{\epsilon\omega}\hat{\boldsymbol{e}}_z.\end{aligned} \tag{B5}$$

Therefore, the conservation law for angular momentum and energy associated with the magnetic quantum number m in the asymptotic region in CP fields is given by

$$E = \epsilon\omega(L_z - m) - I_p - U_p. \tag{B6}$$

For EP fields, the angular momentum [Eq. (B3)] in the asymptotic region is

$$L_z = \left(x_0 - \frac{A_0}{\omega}\right)(k - \epsilon A_0), \tag{B7}$$

where x_0 is given in Eq. (A10), and the energy [Eq. (B4)] in the asymptotic region is

$$E = \tfrac{1}{2}(k - \epsilon A_0)^2. \tag{B8}$$

Therefore, in EP fields, the conservation law for angular momentum and energy associated with the magnetic quantum number m in the asymptotic region is established through the dependence of the angular momentum and energy on the auxiliary momentum k, given by Eqs. (B7) and (B8).

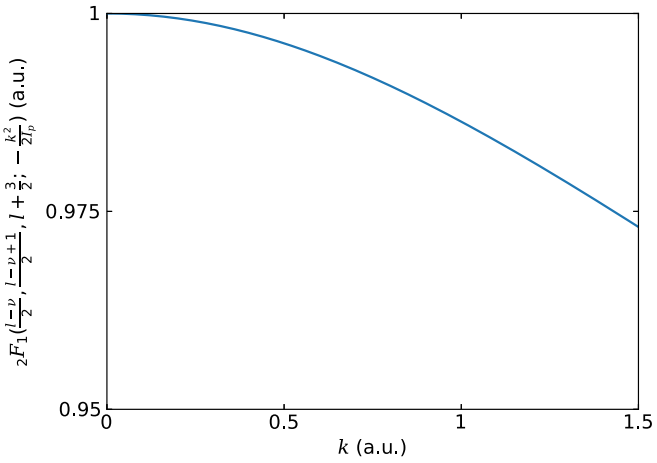

FIG. 5. The hypergeometric function $_2F_1(\frac{l-\nu}{2}, \frac{l-\nu+1}{2}, l+\frac{3}{2}; -\frac{k^2}{2I_p})$ for $2p_\pm$ orbitals of Ne.

APPENDIX C: ASYMPTOTIC FORM OF THE INITIAL WAVE FUNCTION IN MOMENTUM SPACE

In this Appendix, we briefly describe the simplification of the asymptotic form of the initial wave function in the momentum space [Eq. (6)]. For the $2p_\pm$ orbitals of Ne, since the constant term in the asymptotic form of the initial wave function in momentum space does not impact the overall dynamics, it can be safely ignored in later calculations. Furthermore, as illustrated in Fig. 5, the Gauss hypergeometric function exhibits slow variation within the momentum range [0,1.5], and we thus approximate it as a k-independent constant term. Therefore,

$$\tilde{\psi}_\pm(\boldsymbol{k}) \sim \frac{kY_{lm}(\hat{\boldsymbol{k}})}{(k^2+2I_p)^{\nu+1}}, \tag{C1}$$

where the spherical harmonics $Y_{lm}(\hat{\boldsymbol{k}})$ can be further simplified to

$$Y_{lm}(\hat{\boldsymbol{k}}) = \mp\sqrt{\frac{3}{8\pi}}\sin(\theta_k)e^{im\phi_k} \sim \sin(\theta_k)e^{im\phi_k} \tag{C2}$$

for $l=1$, $m=\pm1$. Substituting Eq. (C2) into Eq. (C1), we obtain

$$\tilde{\psi}_\pm(\boldsymbol{k}) \sim \frac{k\sin(\theta_k)e^{im\phi_k}}{(k^2+2I_p)^{\nu+1}} = \frac{\sqrt{k_x^2+k_y^2}e^{im\phi_k}}{(k^2+2I_p)^{\nu+1}} = \frac{k_x+imk_y}{(k^2+2I_p)^{\nu+1}}. \tag{C3}$$

[1] A. Sommerfeld and G. Schur, Über den Photoeffekt in der K-Schale der Atome, insbesondere über die Voreilung der Photoelektronen, Ann. Phys. **396**, 409 (1930).

[2] W. Becker, F. Grasbon, R. Kopold, D. Milošević, G. Paulus, and H. Walther, Above-threshold ionization: From classical features to quantum effects, Adv. At. Mol. Opt. Phys. **48**, 35 (2002).

[3] D. N. Fittinghoff, P. R. Bolton, B. Chang, and K. C. Kulander, Observation of nonsequential double ionization of helium with optical tunneling, Phys. Rev. Lett. **69**, 2642 (1992).

[4] F. Krausz and M. Ivanov, Attosecond physics, Rev. Mod. Phys. **81**, 163 (2009).

[5] J. Kaushal and O. Smirnova, Nonadiabatic Coulomb effects in strong-field ionization in circularly polarized laser fields, Phys. Rev. A **88**, 013421 (2013).

[6] I. Barth and M. Lein, Numerical verification of the theory of nonadiabatic tunnel ionization in strong circularly polarized laser fields, J. Phys. B **47**, 204016 (2014).

[7] J. Kaushal, F. Morales, and O. Smirnova, Opportunities for detecting ring currents using an attoclock setup, Phys. Rev. A **92**, 063405 (2015).

[8] X. Zhu, P. Lan, K. Liu, Y. Li, X. Liu, Q. Zhang, I. Barth, and P. Lu, Helicity sensitive enhancement of strong-field ionization in circularly polarized laser fields, Opt. Express **24**, 4196 (2016).

[9] M.-M. Liu, M. Li, Y. Shao, M. Han, Q. Gong, and Y. Liu, Effects of orbital and coulomb potential in strong-field nonadiabatic tunneling ionization of atoms, Phys. Rev. A **96**, 043410 (2017).

[10] K. Liu, M. Li, W. Xie, K. Guo, S. Luo, J. Yan, Y. Zhou, and P. Lu, Revealing the effect of atomic orbitals on the phase distribution of an ionizing electron wave packet with circularly polarized two-color laser fields, Opt. Express **28**, 12439 (2020).

[11] D. Trabert, N. Anders, A. Geyer, M. Hofmann, M. S. Schöffler, L. P. H. Schmidt, T. Jahnke, M. Kunitski, R. Dörner, and S. Eckart, Angular dependence of the Wigner time delay upon strong-field ionization from an aligned p orbital, Phys. Rev. Res. **5**, 023118 (2023).

[12] G. Porat, G. Alon, S. Rozen, O. Pedatzur, M. Krüger, D. Azoury, A. Natan, G. Orenstein, B. Bruner, M. Vrakking, and N. Dudovich, Attosecond time-resolved photoelectron holography, Nat. Commun. **9**, 2805 (2018).

[13] M. Han, P. Ge, Y. Fang, X. Yu, Z. Guo, X. Ma, Y. Deng, Q. Gong, and Y. Liu, Unifying tunneling pictures of strong-field ionization with an improved attoclock, Phys. Rev. Lett. **123**, 073201 (2019).

[14] P. Ge, Y. Dou, M. Han, Y. Fang, Y. Deng, C. Wu, Q. Gong, and Y. Liu, Spatiotemporal imaging and shaping of electron wave functions using novel attoclock interferometry, Nat. Commun. **15**, 497 (2024).

[15] Y. Li, P. Lan, H. Xie, M. He, X. Zhu, Q. Zhang, and P. Lu, Nonadiabatic tunnel ionization in strong circularly polarized laser fields: Counterintuitive angular shifts in the photoelectron momentum distribution, Opt. Express **23**, 28801 (2015).

[16] S. Eckart, M. Kunitski, M. Richter, A. Hartung, J. Rist, F. Trinter, K. Fehre, N. Schlott, K. Henrichs, L. P. H. Schmidt, T. Jahnke, M. Schöffler, K. Liu, I. Barth, J. Kaushal, F. Morales, M. Ivanov, O. Smirnova, and R. Dörner, Ultrafast preparation and detection of ring currents in single atoms, Nat. Phys. **14**, 701 (2018).

[17] I. Barth and O. Smirnova, Nonadiabatic tunneling in circularly polarized laser fields: Physical picture and calculations, Phys. Rev. A **84**, 063415 (2011).

[18] I. Barth and O. Smirnova, Nonadiabatic tunneling in circularly polarized laser fields. II. Derivation of formulas, Phys. Rev. A **87**, 013433 (2013).

[19] T. Herath, L. Yan, S. K. Lee, and W. Li, Strong-field ionization rate depends on the sign of the magnetic quantum number, Phys. Rev. Lett. **109**, 043004 (2012).

[20] K. Liu, H. Ni, K. Renziehausen, J.-M. Rost, and I. Barth, Deformation of atomic $p_{\pm}$ orbitals in strong elliptically polarized laser fields: Ionization time drifts and spatial photoelectron separation, Phys. Rev. Lett. **121**, 203201 (2018).

[21] K. Liu, M. Li, W. Xie, Y. Qin, K. Guo, J. Yan, K. Liu, Y. Zhou, and P. Lu, Laser-induced deformation of atomic $p_{\pm}$ orbitals in orthogonally polarized two-color laser fields, J. Opt. Soc. Am. B **39**, 1557 (2022).

[22] L. V. Keldysh, Ionization in the field of a strong electromagnetic wave, Sov. Phys. JETP **20**, 1307 (1965).

[23] F. H. Faisal, Multiple absorption of laser photons by atoms, J. Phys. B **6**, L89 (1973).

[24] H. R. Reiss, Effect of an intense electromagnetic field on a weakly bound system, Phys. Rev. A **22**, 1786 (1980).

[25] S. V. Popruzhenko, Keldysh theory of strong field ionization: History, applications, difficulties and perspectives, J. Phys. B **47**, 204001 (2014).

[26] K. Amini *et al.*, Symphony on strong field approximation, Rep. Prog. Phys. **82**, 116001 (2019).

[27] A. Jašarević, E. Hasović, R. Kopold, W. Becker, and D. Milošević, Application of the saddle-point method to strong-laser-field ionization, J. Phys. A **53**, 125201 (2020).

[28] D. Milošević, G. Paulus, D. Bauer, and W. Becker, Above-threshold ionization by few-cycle pulses, J. Phys. B **39**, R203 (2006).

[29] D. Milošević, A. Jašarević, D. Habibović, E. Hasović, A. Čerkić, and W. Becker, Asymptotic methods applied to integrals occurring in strong-laser-field processes, J. Phys. A **57**, 393001 (2024).

[30] C. Figueira de Morisson Faria, H. Schomerus, and W. Becker, High-order above-threshold ionization: The uniform approximation and the effect of the binding potential, Phys. Rev. A **66**, 043413 (2002).

[31] A. S. Jašarević, E. Hasović, and D. B. Milošević, Modified saddle-point method applied to high-order above-threshold ionization and high-order harmonic generation: Slater-type versus asymptotic ground-state wave function, Phys. Rev. A **109**, 043114 (2024).

[32] P. Salieres, B. Carre, L. Le Deroff, F. Grasbon, G. G. Paulus, H. Walther, R. Kopold, W. Becker, D. B. Milosevic, A. Sanpera, and M. Lewenstein, Feynman's path-integral approach for intense-laser-atom interactions, Science **292**, 902 (2001).

[33] H. Ni, U. Saalmann, and J.-M. Rost, Tunneling ionization time resolved by backpropagation, Phys. Rev. Lett. **117**, 023002 (2016).

[34] H. Ni, U. Saalmann, and J.-M. Rost, Tunneling exit characteristics from classical backpropagation of an ionized electron wave packet, Phys. Rev. A **97**, 013426 (2018).

[35] H. Ni, N. Eicke, C. Ruiz, J. Cai, F. Oppermann, N. I. Shvetsov-Shilovski, and L.-W. Pi, Tunneling criteria and a nonadiabatic term for strong-field ionization, Phys. Rev. A **98**, 013411 (2018).

[36] Y. Ma, H. Ni, and J. Wu, Attosecond ionization time delays in strong-field physics, Chin. Phys. B **33**, 013201 (2024).

[37] Y. Ma, H. Ni, Y. Li, F. He, and J. Wu, Subcycle conservation law in strong-field ionization, Ultrafast Sci. **4**, 0071 (2024).

[38] J. Dubois, C. Lévêque, J. Caillat, R. Taïeb, U. Saalmann, and J.-M. Rost, Energy conservation law in strong-field photoionization by circularly polarized light, Phys. Rev. A **109**, 013112 (2024).

[39] B. Feuerstein and U. Thumm, On the computation of momentum distributions within wavepacket propagation calculations, J. Phys. B **36**, 707 (2003).

[40] X. Wang, J. Tian, and J. H. Eberly, Extended virtual detector theory for strong-field atomic ionization, Phys. Rev. Lett. **110**, 243001 (2013).

[41] X. Wang, J. Tian, and J. Eberly, Virtual detector theory for strong-field atomic ionization, J. Phys. B **51**, 084002 (2018).

[42] R.-H. Xu and X. Wang, Extended virtual detector theory including quantum interferences, AIP Adv. **11**, 025124 (2021).

[43] G. F. Gribakin and M. Y. Kuchiev, Multiphoton detachment of electrons from negative ions, Phys. Rev. A **55**, 3760 (1997).

[44] Y. Ma, J. Zhou, P. Lu, H. Ni, and J. Wu, Influence of nonadiabatic, nondipole and quantum effects on the attoclock signal, J. Phys. B **54**, 144001 (2021).

[45] X. Mao, H. Ni, X. Gong, J. Burgdörfer, and J. Wu, Subcycle-resolved strong-field tunneling ionization: Identification of magnetic dipole and electric quadrupole effects, Phys. Rev. A **106**, 063105 (2022).

[46] X. Mao, H. Ni, and J. Wu, Visualization of subcycle nonadiabatic-nondipole coupling in strong-field ionization, Phys. Rev. A **110**, 063113 (2024).

[47] Y. Ma, X. Mao, L. Kong, Q. Liu, H. Ni, and J. Wu, Distinct role of electric field and vector potential in strong-field tunneling ionization, Phys. Rev. A **111**, 033103 (2025).

[48] M. Klaiber, Q. Z. Lv, S. Sukiasyan, D. Bakucz Canário, K. Z. Hatsagortsyan, and C. H. Keitel, Reconciling conflicting approaches for the tunneling time delay in strong field ionization, Phys. Rev. Lett. **129**, 203201 (2022).

[49] J.-P. Wang and F. He, Tunneling ionization of neon atoms carrying different orbital angular momenta in strong laser fields, Phys. Rev. A **95**, 043420 (2017).

[50] Q. Zhang, G. Basnayake, A. Winney, Y. F. Lin, D. Debrah, S. K. Lee, and W. Li, Orbital-resolved nonadiabatic tunneling ionization, Phys. Rev. A **96**, 023422 (2017).

[51] Y. H. Kim, I. A. Ivanov, and K. T. Kim, Classical backpropagation for probing the backward rescattering time of a tunnel-ionized electron in an intense laser field, Phys. Rev. A **104**, 013116 (2021).

[52] H. Ni, S. Brennecke, X. Gao, P.-L. He, S. Donsa, I. Březinová, F. He, J. Wu, M. Lein, X.-M. Tong, and J. Burgdörfer, Theory of subcycle linear momentum transfer in strong-field tunneling ionization, Phys. Rev. Lett. **125**, 073202 (2020).

[53] C. T. L. Smeenk, L. Arissian, B. Zhou, A. Mysyrowicz, D. M. Villeneuve, A. Staudte, and P. B. Corkum, Partitioning of the

linear photon momentum in multiphoton ionization, Phys. Rev. Lett. **106**, 193002 (2011).

[54] M.-X. Wang, S.-G. Chen, H. Liang, L.-Y. Peng, H. Liang, and L.-Y. Peng, Review on non-dipole effects in ionization and harmonic generation of atoms and molecules, Chin. Phys. B **29**, 013302 (2020).

[55] J. Maurer and U. Keller, Ionization in intense laser fields beyond the electric dipole approximation: Concepts, methods, achievements and future directions, J. Phys. B **54**, 094001 (2021).

[56] H. Ni, Modification of the saddle-point equation for strong-field ionization from atomic p orbitals, Zenodo, 2025, https://doi.org/10.5281/zenodo.14646437.